Studying the Properties of Higher-Order Modes in Gravitational Wave Emission from Binary Black Hole Merger Events

LIGO SURF 2020 Final Report

Jennifer Sanchez

Physics Department, California State University, Fullerton

Mentors: Dr. Alan J. Weinstein and Dr. Colm Talbot

LIGO Laboratory, Physics Department, California Institute of Technology

(Dated: October 17, 2020)

Advanced LIGO and Advanced Virgo have confidently detected gravitational wave signals from 10 binary black hole mergers and one merger from a binary neutron star. Each observation contains encoded information about the physical properties of the binary system. As the detectors continue to improve their sensitivity, these developments will allow us to detect rarer systems and make more confident statements regarding their source properties. In order to fully characterize the gravitational wave observations, we rely on numerical and analytical models that approximate the signal waveforms from the emitted source as specified by the source parameters (masses, spins, sky location, etc.). The dominant emission frequency of gravitational waves from a compact binary coalescence is at twice the orbital frequency; however, recently published events have demonstrated subdominant higher-order harmonic contributions. The primary focus of this study is to explore higher-order modes in gravitational wave signals with newly improved signal models.

I. INTRODUCTION

Black hole binaries, along with other compact binaries, are responsible for the gravitational waves that have been detected by the LIGO Scientific Collaboration [1] and Virgo [2]. Since 2015, the year in which the first gravitational wave was detected, there have been 9 additionally confirmed gravitational waves from binary black hole mergers, one merger from a binary neutron star [3], and 56 candidate detections of gravitational wave signals from LIGO and Virgo's 3rd observing run, O3, in 2019-2020 [4]. The current operational detectors are only able to observe the closest and loudest sources that exist in the local universe. Now that gravitational waves can be detected and analyzed, this is only the beginning for gravitational wave science.

During the third observing run of Advanced LIGO and Advanced Virgo, all three interferometers operated at unprecedented sensitivity [5]. With the observations of 67 gravitational wave signals [4], the need for accurate models of the emitted sources is essential. Observations made during O3 have provided the first evidence for binaries with unequal mass and misaligned spins [6].

Parameters describing the merging binaries are inferred using Bayesian inference by comparing template families to the data. Earlier parametrized waveform families (or models) did not include higher-order multipoles; however, the recent observations require waveform models including higher-order emission multipoles. Not only will these models provide us with information regarding the inspiral, merger, and ringdown of the source, but will also allow tests of general relativity [7], measurements of the underlying population of compact objects [8] and the expansion history of the Universe [9].

In this report, we will be discussing the properties of the event GW190412 which was observed by both Advanced LIGO and Advanced Virgo detectors [6]. The signal waveform included its signature dominant quadrupole radiation; however, it also contained *detectable* higher harmonics which will provide us with a greater insight to the dynamics of coalescing binary black holes.

II. SOURCE PROPERTIES

The source properties we have been studying prior to O3 included: masses (m_1 and m_2), spins of the black holes in the binary ($\vec{S_1}$ and $\vec{S_2}$), the sky location, luminosity distance (D_L), binary orbital orientation, and time (t_c) and phase (ϕ_c) of coalescence. All of these properties comprise to a total of 15 parameters. Specifying these parameters allows one to predict the signal waveform that may be present in the detector network data. These 15 parameters can be can be divided into intrinsic and extrinsic parameters (see Fig. 1).

The intrinsic parameters depend only on the source and are independent of the observer. These parameters consist of the two mass components (m_1 and m_2) and the six spin components for vectors $\vec{S_1}$ and $\vec{S_2}$. The extrinsic parameters are the parameters that depend on the observer. This includes the sky position which is measured in celestial coordinates (α, δ), luminosity distance (D_L), time and reference phase at coalescence (t_c and φ_c), inclination angle (θ_{JN}) which is the angle between the total angular momentum ($\hat{J}$) and the line of sight of the observer ($\hat{N}$), and lastly the polarization angle (ψ). If we look at a binary system in the sky, and the angle between $\hat{N}$ and $\hat{L}$ is $0°$, we say it is "face on." If the angle
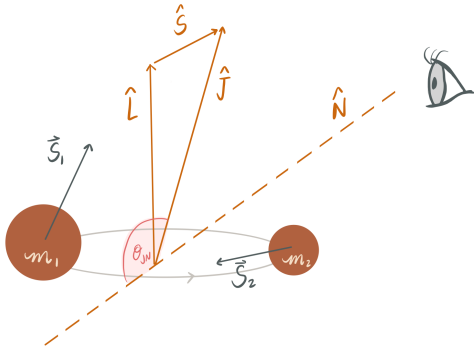
FIG. 1. This plot illustrates how the 15 binary black hole parameters are defined in this study. The line of sight of the observer is represented by the normal vector $\hat{N}$, $\hat{L}$ and $\hat{J}$ are the orbital angular momentum and total angular momentum vectors respectively, and $\vec{S}_1$ is the spin vector of the larger black hole.

is $90°$, we say it is "edge on", and anything in between is viewed as an ellipse. This ellipse has an azimuthal angle known as the polarization angle.

Gravitational waves are transverse waves that have two independent polarization states denoted by h_+ and $h_\times$, where $h_\times$ has its principle axis rotated $45°$ with respect to h_+ [10]. With these two polarizations at hand, we can write the strain of the gravitational wave as the complex quantity, $h = h_+ - ih_\times$ [11]. According to the works of pioneering scientists, another fundamental property of gravitational waves from compact binaries is that they are dominantly quadrupolar. While gravitational radiation often includes the lowest order radiation term, the quadrupole radiation, there are predictions that include higher multipoles [12]. However, higher multipoles, which are terms above the dominant, quadrupolar term, are particularly complex to infer from a gravitational wave signal produced by near equal mass binaries [6].

Recently, signal waveform families have been extended to include higher-order multipoles. The dominant multipole is $(l, m) = (2, 2)$ described by a spin-weighted spherical harmonic, $_{-2}Y_{lm}(\theta, \phi)$, where θ and ϕ are the emission angles toward the observer relative to the orbital angular momentum, ℓ. We can describe the multipolar decomposition as:

$$h_+ - ih_x = \sum_{\ell=2}^{\infty} \sum_{m=-\ell}^{\ell} \frac{h(t, \lambda)}{D_L} {}_{-2}Y_{\ell m}(\theta, \phi) \qquad (1)$$

where t denotes the time, λ represents the intrinsic parameters such as the black holes' masses and spins, D_L represents the luminosity distance from the observer, and (θ, ϕ) are the emission angles relative to the total angular momentum of the source $\vec{J}$ so that $\theta = \theta_{JN}$. Lastly, we recognize that, $h = h_+ - ih_\times$ is in the form of a complex sinusoidal, $\cos(\omega t) - i\sin(\omega t)$ or similarly $e^{-i\omega t}$.

The event's mass ratio, q, is an important factor to consider since it affects the geometry of the source. General relativity predicts that when the masses of the binary are increasingly unequal, the higher-order multipoles are increasingly important.

Another contributor to higher multipoles is the orientation of the source. Higher-order multipoles are more prominent when θ is different from 0 or π, also said to be "face on." As a result of the degeneracy between θ_{JN} and D_L, higher multipoles allow us to break this degeneracy which permits us to tighten constrains on both parameters [6].

III. HIGHER MULTIPOLES

It is critical to have theoretical models of a gravitational wave signals that incorporate all of the features present in the measurements made by Advanced LIGO and Virgo. Typically, these models include the dominant $(l, m) = (2, 2)$ mode; however, this is not always the case. When the sources have a mass ratio close to one, these models are sufficient to analyze the source parameters of the system, such as distance and inclination. However, when the black hole binary contains an unequal mass ratio, models incorporating subdominant multipoles may be remarkably more accurate.

In Fig. 2, we can see the strain data from GW190412, the fractional change in displacement between two nearby masses due to the gravitational wave, taken by the LIGO Livingston detector. The time-frequency representation of GW190412 shows the signal to noise ratio (SNR, informally referred to as the "loudness") of the event in each detector. The signal present strongly implies that the source has an astrophysical origin rather than local detector noise [6].
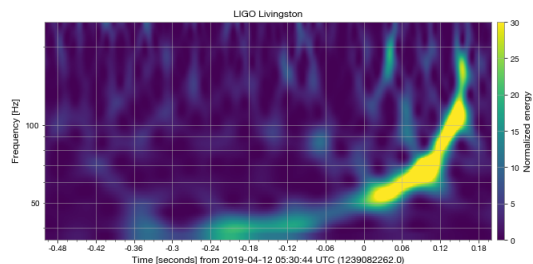

FIG. 2. Spectrogram of GW190412 in LIGO Livingston. The x-axis represents time while the y-axis represents the frequency of the gravitational wave signal. In this time-frequency representation, we can see the energy given a specific frequency at a specific time. The increase in frequency and energy over time is the result of the inspiraling black holes followed by their merger.

What makes this event so unique is the notable asymmetry of the black hole masses, that is – the mass of one of the black holes is roughly three times heavier than the other [6]. This makes GW190412 a favorable system for identifying the presence of higher-order multipoles.

Previously, nearly all detected binary systems were consistent with having zero net aligned spin; however, it was found that GW190412 has significant net positive aligned spin χ_{eff} [6]. On account of the unequal mass ratio, we can apply a constraint on the spin of the larger black hole. Making use of higher-order multipoles in the model waveforms will allow us to make more precise measurements of all the parameters including the distance and inclination of the system, also shown in Fig. 3. General relativity predictions are precise predictions for the content and strength of higher-order multipoles. In this study, we investigate the degree to which the predictions accurately describe the data.
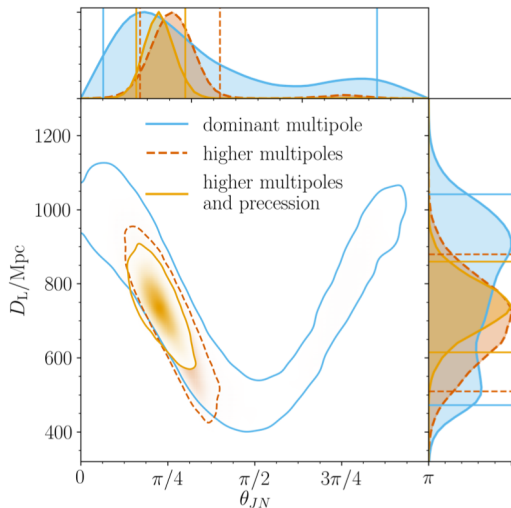
FIG. 3. Posterior distribution of GW190412 luminosity distance (D_L) and inclination (θ_{JN}). We see that by using models that include the dominant multipole, higher mulitpoles, and higher multipoles and precession, we are able to constrain D_L and θ_{JN}. Degeneracy breaks when higher-order modes are included which allows us to improve our accuracy [[6]].

IV. GRAVITATIONAL WAVEFORM MODELLING

The three waveform families currently used to accurately model gravitational waves for binary systems are the phenomenological waveforms, effective-one-body waveforms, and numerical relativity surrogates. The phenomenological and effective-one-body waveforms model the inspiral, merger, and ringdown of the gravitational wave signal[13]; however, the numerical relativity surrogates are typically limited before the merger and ringdown [14].

A. Phenomenological models

The phenomenological waveforms focus on modeling the inspiral, merger, and ringdown (IMR) of a gravita-

tional wave signal without providing equations of motions for the black hole dynamics [12]. The phenomenological waveform model is typically created in the frequency domain which makes it computationally quick to evaluate for data analysis applications [12]. The newest edition of the phenomenological waveform models are IMRPhenomPv3HM and IMRPhenomXPHM. IMRPhenomPv3HM and IMRPhenomXPHM tracks precession and includes higher modes [12].

B. Effective-one-body models

Effective-one-body (EOB) waveform models attempt to unify the quasicircular inspiral, merger, and ringdown of the binary by including post-Newtonian theory and black hole perturbation theory [13]. The newest EOB model, SEOBNRv4PHM, includes both spin precession and higher multipoles [13]. The numerical relativity waveforms which have been used to calibrate EOB waveforms included mass ratios $q = 1 - 4$ and dimensionless spins, $\chi_{1,2}$ up to 0.9 [13].

C. Numerical relativity surrogate models

Numerical relativity simulations are able to accurately model the complex morphology of binary black hole mergers; however, the simulations are computationally expensive. Numerical relativity based surrogates are an alternative approach as they are substitute models for the outputs of these simulations. These models use numerical relativity simulated waveforms to reconstruct underlying phenomenology [14]. The newest numerical relativity surrogate mode, NRSur7dq4 begins ∼20 orbits before merger and includes all $\ell \leq 4$ spin-weighted spherical harmonic modes [14]. The seven parameters in the precessing binary black hole system are the mass ratio ($q = m_1/m_2$) where $m_1 \geq m_2$ and the two spin vectors χ_1 and χ_2 where χ_1 represents the heavier black hole [14]. To generate a waveform in the time domain using the NRSur7dq4 model, parameters are required to calculate the waveform, like all other models. These inputs include, the system's mass ratio, dimensionless spin vector of the two black holes, total mass of the binary ($m_1 + m_2$), maximum ℓ index for modes to use, reference frequency, initial frequency, distance, and sample rate.

D. Phenomenology of higher-order multipoles

To explore the detectability of higher-order modes in varying parameter space, in Fig. 4, I show the real part of the $(\ell, m) =$(2,1), (2,2), (3,2), (3,3), and (4,4) modes in the time-domain. Fig. 4 was generated using the NRSur7dq4 model with parameters given in Table. I. We see that in both the time and frequency-domain (Fig. 5), the (2,2) mode has the highest amplitude while the features

in the (3,3) mode occur at 1.5 times the frequency as for the (2,2) mode and the (4,4) mode, with the lowest amplitude, is at twice the frequency of the (2,2) mode.
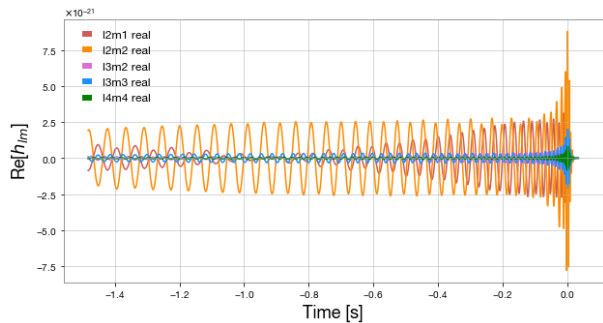

FIG. 4. The real part of the (2,1), (2,2), (3,2), (3,3), and (4,4) modes of the NRSur7dq4 surrogate model waveform. To produce this figure, all waveforms used a q=4, χ_1=[-0.2, 0.4, 0.1], and χ_2 =[-0.5, 0.2, -0.4]. Each waveform has been time shifted so its total amplitude appears at t = 0.
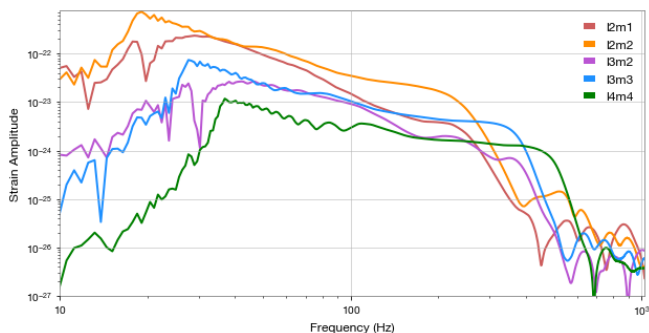

FIG. 5. The (2,1), (2,2), (3,2), (3,3), and (4,4) modes of the NRSur7dq4 waveform in the frequency domain. The wiggles at the low frequency are due to the fact that the time-domain waveform is generated with a starting frequency of 20 Hz for the (2,2) mode. The strain amplitudes at the lower frequencies are thus artificially cut off.

To analyze gravitational wave signals, it is often helpful to convert the waveform to the frequency-domain. This can be accomplished using a fast Fourier transform. In order to mitigate numerical artifacts, I apply a Tukey window function to the time-domain data before performing the fast Fourier transform. This windowing function reduces the effects of spectral leakage and Gibbs phenomena [15].

TABLE I. Parameters used to evaluate all waveforms

q	χ_1	χ_2,	$M_\odot$	d (Mpc)	ℓ_{max}
4	[-0.2, 0.4, 0.1]	[-0.5, 0.2, -0.4]	70	100	4

Fig. 5 shows that as the mode of the waveform increases, the amplitude decreases. The oscillations located at lower and higher frequencies are likely an artefact of signal processing and Gibbs phenomenon which could

be further reduced with a more careful choice of window function. Looking at the orange line representing the (2,2) mode, the inspiral occurs between the minimum simulated frequency, 20 to ∼200Hz. The plunge and merger then appears at 200-250Hz where the curve flattens.

In Fig. 6, 7, and 8, I present three Q transforms which show the chirp of the signal with their respective mode. We note that the frequency behaves accordingly to m which means the m=4 mode is 4/3 of the frequency of m=3 and twice the frequency of m=2. Similarly, these findings can also be concluded from the frequency domain representation of the signal (Fig. 5).
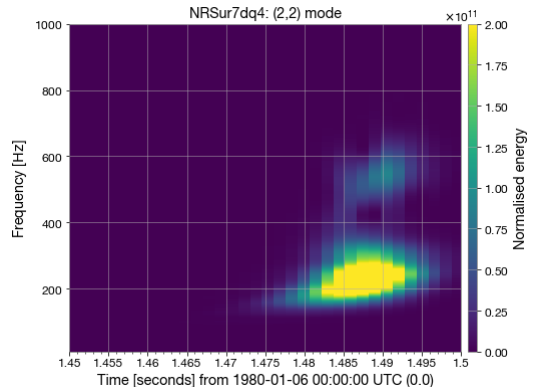

FIG. 6. Q transform of the (2,2) mode using the NRSur7dq4 waveform model. The merger of the signal has a frequency of ∼200-250 Hz.
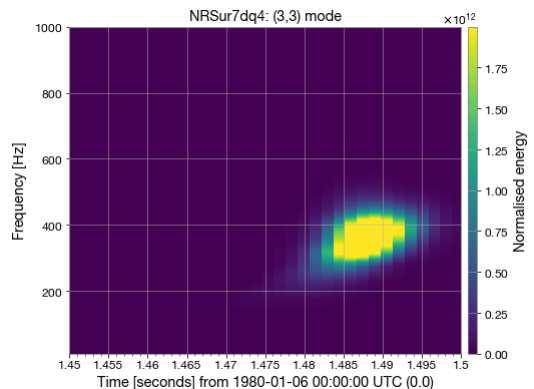

FIG. 7. Q transform of the (3,3) mode using the NRSur7dq4 waveform model. The merger of the signal has a frequency of ∼300-410 Hz.

V. COMPARISON OF HIGHER-MODE MULTIPOLES FOR GW190412

In this section, I compare two waveform models, IMR-PhenomPv3HM and SEOBNRv4PHM, using GW190412 posterior samples for the source properties. I used the
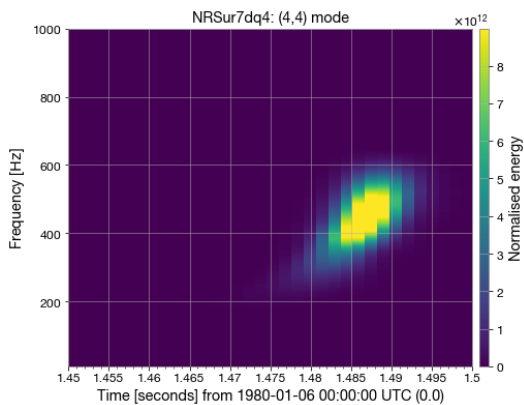
FIG. 8. Q transform of the (4,4) mode using the NRSur7dq4 waveform model. The merger of the signal has a frequency of ∼400-500 Hz.

'mode_array' argument in `PyCBC` which allows you to chose which (l, m) modes to include when generating a waveform. NRSur7dq4 could not be used in this comparison since it was not used for the GW190412 analysis (as it was not yet fully tested and reviewed at the time that the analysis was performed).

A. IMRPhenomPv3HM

Fig. 9 shows the GW190412 waveform in the time domain generated using the posterior samples for the source properties [16]. Posterior samples are important to include in the parameters of the waveform since they provide a more accurate representation of the signal which corresponds to a given model and detector. There are noticeable indications of amplitude modulation which is caused by the spin-induced orbital precession of GW190412.
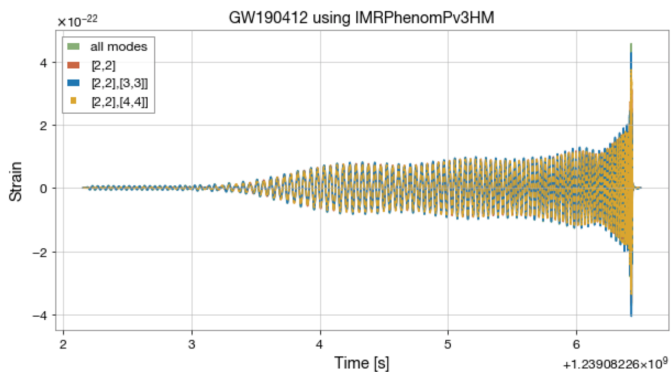

FIG. 9. Time-domain waveforms of IMRPhenomPv3HM showing the higher-order multipoles. These waveforms were generated using the posterior samples for the source parameters [16].

Looking at the waveform in the frequency-domain as

shown in Fig. 10, we see the amplitude wiggles during the inspiral phase which are due to the spin orbit precession of the binary. We also note the merger of $(2, 2)$ mode is at $f \approx 400$ Hz, the $(3, 3)$ mode at $f \approx 600$ Hz, and the $(4, 4)$ mode at $f \approx 800$ Hz.
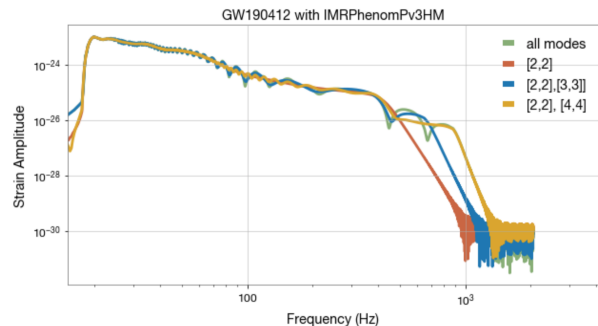

FIG. 10. Frequency-domain waveforms of IMRPhenomPv3HM showing the effects of higher multipoles. These waveforms were produced using the posterior samples for the source parameters [16].

B. SEOBNRv4PHM

I proceeded to compare the higher-order multipoles using the SEOBNRv4PHM waveform model which was produced using the GW190412 posterior samples for source properties[16]. Fig. 11 shows that including the $(3, 3)$ mode makes a visible change. In fact, LIGO scientists explain in the GW190412 discovery paper that the $(3, 3)$ mode makes significant measurable contributions [6]. The small green peak at $t = 0$ in Fig. 11 is evidence that the second most important multipole is the $(l, |m|) = (3, 3)$ multipole.
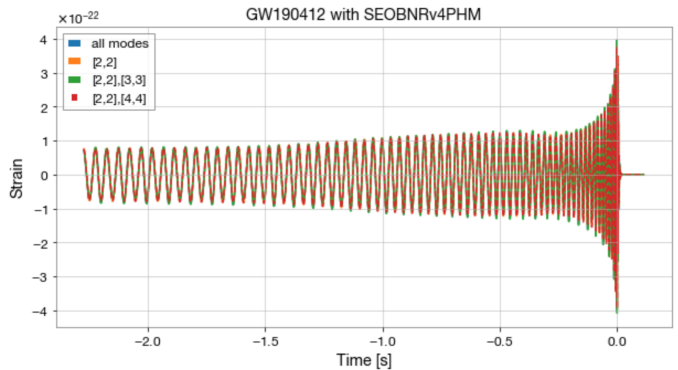

FIG. 11. Time-domain waveforms of SEOBNRv4PHM showing the higher-order multipoles. These waveforms were generated using the posterior samples for the source parameters [16].

Fig. 12 shows the waveforms in the frequency-domain with their respective multipoles. The merger of the $(2, 2)$

mode is at $f \approx 400$ Hz, the $(3,3)$ mode at $f \approx 600$ Hz, and the $(4,4)$ mode at $f \approx 800$ Hz. We note that unlike the IMRPhenomPv3HM frequency-domain results, the dips in frequency near merger are not as steep. This could mean that perhaps that different waveforms models give different predictions for how much interference there is between multipole contributions.
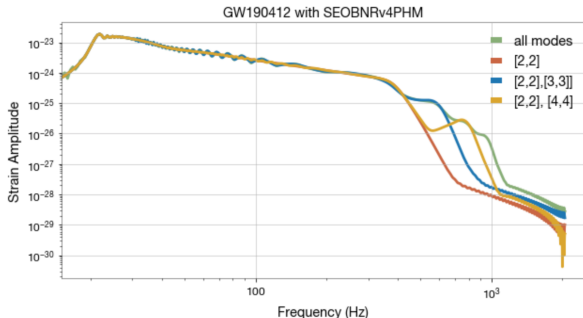

FIG. 12. Frequency-domain waveforms of SEOBNRv4PHM showing the effects of higher multipoles. These waveforms were produced using the posterior samples for the source parameters [16].

C. IMRPhenomPv3HM and SEOBNRv4PHM

The next comparison is between the two waveforms produced by IMRPhenomPv3HM and SEOBNRv4PHM using two sets of the posterior samples for GW190412. I included the antenna response function when generating these waveforms for this study. Gravitational wave detectors produce a time series $h(t)$ which contains the response function (F_+ and $F_\times$) of the detector to each polarization (h_+ and $h_\times$) which can be described as

$$h(t) = F_+(\theta, \phi, \psi)h_+(t) + F_\times(\theta, \phi, \psi)h_\times(t). \quad (2)$$

For this comparison, I used PyCBC's methods [17] to calculate the projection onto the antenna patterns for the LIGO Livingston detector. Additional parameters such as the source's sky location (θ, ϕ) and the corresponding polarization angle are needed (ψ). It is important to transform the two polarisations according to the interferometer antenna patterns because this affects the signal of the gravitational wave as seen by the detector. As shown in Fig. 13, the time domain waveforms for IMRPhenomPv3HM and SEOBNRv4PHM show visible differences in the shape of the waveform models. The varying amplitude of the waveform suggests that the two have different spin modulation effects. We also observe that as the two waveform models approach merger, they agree well in phase but not in amplitude.

In order to determine how well IMRPhenomPv3HM and SEOBNRv4PHM agree with one another, it is often useful to compute the inner product $(h_1|h_2)$ of the

two models. I generated 100 IMRPhenomPv3HM and SEOBNRv4PHM waveforms with parameters given by the 12,513 posterior samples. With IMRPhenomPv3HM defined as h_1, SEOBNRv4PHM as h_2, LIGO Livingston's PSD as $S_n(f)$, and the Fourier transform of $h_1(f)$ as $\tilde{h}_1(f)$, the noise-weighted inner product between $(h_1|h_2)$ is given by

$$(h_1|h_2) = \int_{f_0}^{f_1} \frac{df\tilde{h}_1(f)\tilde{h}_2^*(f)}{S_n(f)} e^{2\pi i \phi_c f t_c} \quad (3)$$

where $f_0 = 20$ Hz and $f_1 = 4096$ Hz [18]. The normalized overlap, which is bounded between zero and one, is defined as

$$\mathcal{O}(h_1, h_2) = \left[\frac{(h_1|h_2)}{(h_1|h_1)^{1/2}(h_2|h_2)^{1/2}} \right]_{max\ t_c, \varphi_c} \quad (4)$$

By producing a histogram of the 100 evaluated overlaps as shown Fig. 14's left historgram, we can see that overall, $\mathcal{O} \geq 0.9$ across the parameter space of GW190412. This result tells us that despite the different waveform shapes in the time domain, there is a strong overlap between the waveforms. We note the two waveforms often had $0.75 \leq \mathcal{O} \leq 0.87$ which demonstrates that both waveforms can overlap well with the data yet not strongly with each other.

The iteration of 100 evaluated overlaps was computed twice more. The first instance, as shown in middle histogram in Fig. 14, was to show the normalized overlap between the 100 IMRPhenomPv3HM waveform pairs computed using 100 different posterior samples. The second instance compares the normalized overlap between 100 SEOBNRv4PHM waveform pairs which are also computed using 100 different posterior samples. The middle histogram in Fig. 14 shows that the overlap is mostly high, $\mathcal{O} \geq 0.92$ while the left histogram in Fig. 14 shows that the overlap is slight higher, $\mathcal{O} \geq 0.93$. These results provide evidence that the waveform models produce consistent outcomes when using different posterior samples from gravitational wave signals.

As shown in Fig. 15, by comparing the aLIGO design sensitivity PSD and the PSD posterior sample for GW190412, we observe clear visible differences. One important difference to note is the slope of the two curves at ~20-50 Hz. As a result, the slope is changing the relative weighting as a function of frequency. The aLIGO design sensitivity PSD will emphasize the lower frequencies which will lead to committing systematic errors that will produce low overlaps as shown in Fig. 16.

VI. REANALYZING GW190412 WITH IMRPHENOMXPHM

I performed an inference of the source properties of GW190412 using Bilby. I included eight seconds of data around the trigger time of event. The waveform model used for this analysis is IMRPhenomXPHM. To study
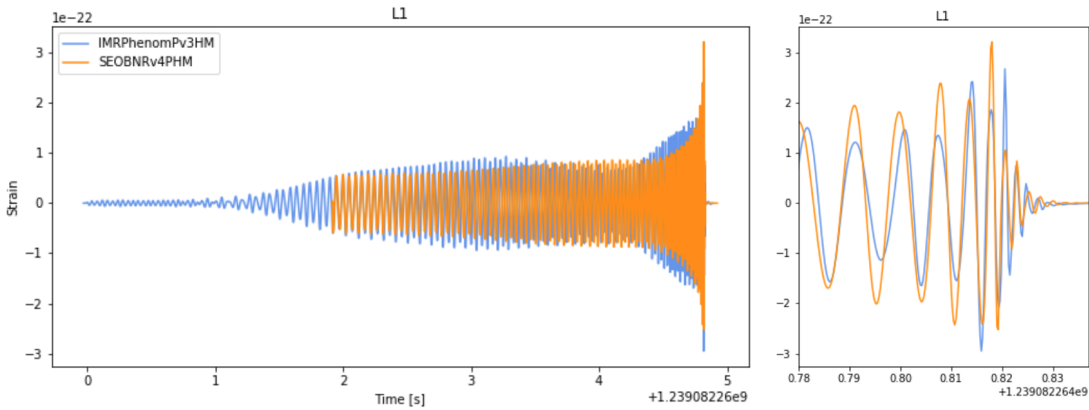
FIG. 13. Time-domain comparison of GW190412 using SEOBNRv4PHM and IMRPhenomPv3HM with posterior samples for the source parameters [16]. Each waveform is projected onto the antenna patterns for the LIGO Livingston detector.
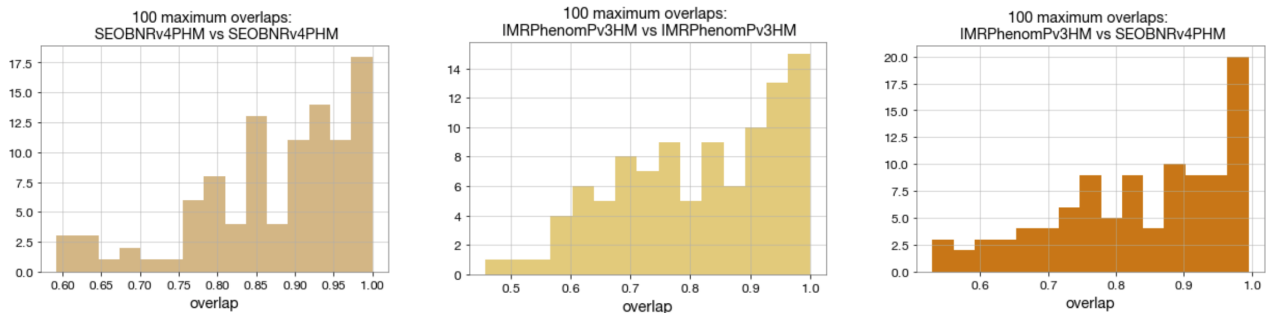

FIG. 14. Three histograms of 100 normalized overlaps between different waveforms. Left: normalized overlaps between IMRPhenomPv3HM and SEOBNRv4PHM waveforms. Middle: normalized overlaps between IMRPhenomPv3HM waveforms. Right: normalized overlaps between SEOBNRv4PHM waveforms. All parameters used to generate the waveforms come from the GW190814 posterior samples for source properties [16].
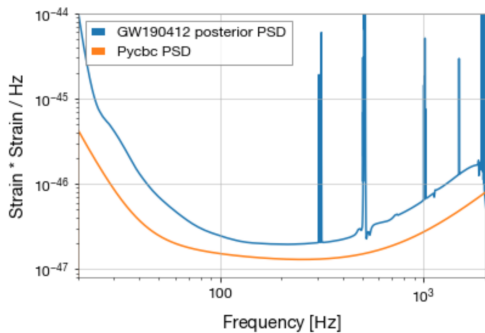

FIG. 15. The strain sensitivity for the LIGO Livingston detector (L1) during O3. Shown is the noise level for the Advanced LIGO design (orange curve) and for the posterior power spectral density for GW190412 (blue curve).

A. Masses

Fig. 17 shows the inferred values of the two masses, m_1 and m_2, of GW190412. This result was obtained using IMRPhenomXPHM which includes both spin orbit precession and higher-order multipoles. The two component masses are $m_1 = 34.66^{+5.89}_{-4.75} M_\odot$ and $m_2 = 9.59^{+1.28}_{-1.1} M_\odot$ while the published masses in the GW190412 discovery paper using the Phenom family are $m_1 = 28.1^{+4.8}_{-4.3} M_\odot$ and $m_2 = 8.8^{+1.5}_{-1.1} M_\odot$ [6]. These black hole mass values are in the range spanned by the events seen in O1 and O2. [3]. An interesting observation is that the mass ratio, $q = 0.28^{+0.09}_{-0.07}$, shown in Fig. 18, is not consistent with the mass ratio ranges from the first two LIGO and Virgo observing runs. GW190412 is the first observed binary black hole that has asymmetric masses.

B. Orientation and spins

Fig. 19 show the posterior probability density for the inclination angle θ_{JN} using IMRPhenomXPHM with and

the effects of higher-order multipoles in the data, the analysis includes IMRPhenomXPHM with higher-order multipoles and IMRPhenomXPHM considering only the quadrupolar $(l, |m|) = (2, 2)$ modes.
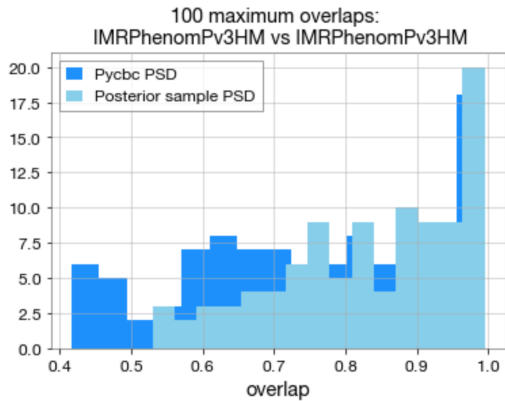
FIG. 16. Overlaps between the IMRPhenomPv3HM waveform model using 100 different source parameter posterior samples for GW190412. Shown is the overlaps using the aLIGO design sensitivity PSD (dark blue histogram) and using the PSD posterior sample (light blue).
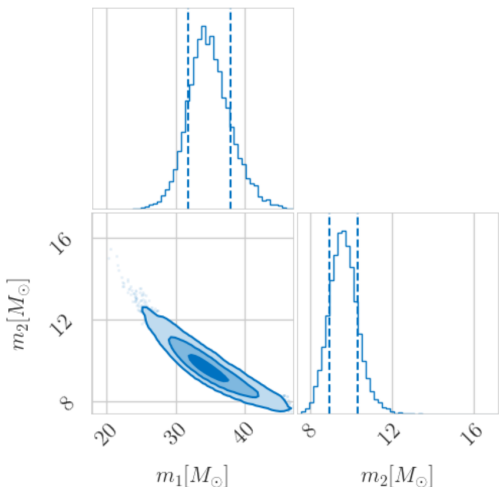

FIG. 17. Posterior probability density of the masses, m_1 and m_2, of GW190412 obtained with IMRPhenomXPHM.
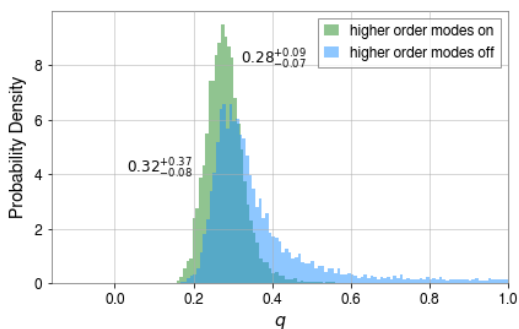

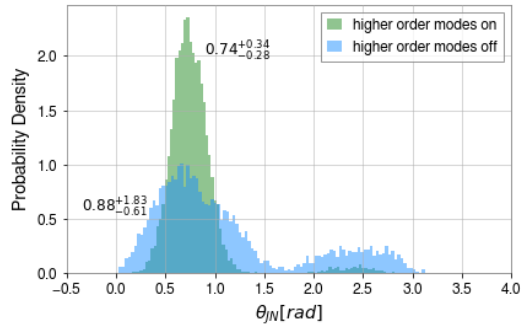FIG. 18. Posterior probability density of the mass ratio, of GW190412 obtained with IMRPhenomXPHM.

FIG. 19. Posterior probability density of the inclination (the angle between the line of sight and total angular momentum), θ_{JN}, of GW190412 obtained with IMRPhenomXPHM with higher-order multipoles. The values on the plot give the median and 90% confidence interval.

without the higher-order multipoles. Comparing the two figures, we note that including higher-order multipoles allows us to constrain the inclination much better than with $(\ell, |m|) = (2,2)$ alone.

The $\chi_{\rm eff}$ parameter is a quantity dependent to the spin alignment of two black holes with their inspiral orbital angular momentum, and to the magnitude of the individual spins, χ_1 and χ_2 (see, e.g.,[19]). This dimensionless number ranges from -1 to 1 and is defined as

$$\chi_{\rm eff} = \frac{m_1 \chi_1 \cos\theta_1 + m_2 \chi_2 \cos\theta_2}{M} \qquad (5)$$

where χ_i represents the dimensionless spin parameter, $\theta_i = \cos^{-1}(\vec{L} \cdot \vec{S_i})$ is the angle between the spin $(\vec{S_i})$ and the orbital angular momentum $(\vec{L})$, and the total mass $M = m_1 + m_2$. When $\chi_{\rm eff} = 1$, this means the spins of the two black holes are aligned with their orbit, $\chi_{\rm eff} = -1$ means the spins are anti-aligned, and $\chi_{\rm eff} \approx 0$ typically means the two black holes have a rotation anti-aligned with one another or non-spinning. The effective spin parameter, as shown in Fig. 20, including higher-order multipoles is $\chi_{\rm eff} = 0.26^{+0.1}_{-0.1}$. The results for this event reveals that its signal has at least one nonzero spin component [6].

While the effective inspiral spin parameter measures the spin components aligned with the orbital angular momentum, the effective precession spin parameter, χ_p, is used to measure the spin components in the orbital plane. This quantity distinguishes how much the spins of the black holes wobble when they are not aligned with orbital plane, also referred to as precession. When there is no precession, $\chi_p = 0$, and there is a maximum precession when $\chi_p = 1$.

In Fig. 21, the posterior probability density of χ_p is shown using IMRPhenomXPHM with and without higher-order multipoles. Including higher-order multipoles, we obtain $\chi_p = 0.24^{+0.19}_{-0.13}$ while $\chi_p = 0.32^{+0.35}_{-0.19}$ when excluding higher-order multipoles. These values tell us that there is in-plane spin despite not having
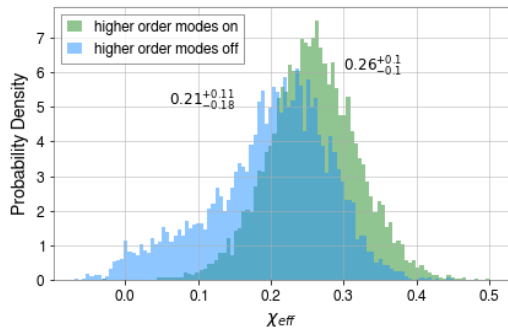
FIG. 20. Posterior probability density of the effective spin, χ_{eff}, with and without higher-order multipoles. The values on the plot give the median and 90% confidence interval.

strong precession. Although we are not able to measure the spins in GW190412 (or any other binary black hole event observed so far) with high precision, by observing more events we hope to make more confident black hole spin measurements.
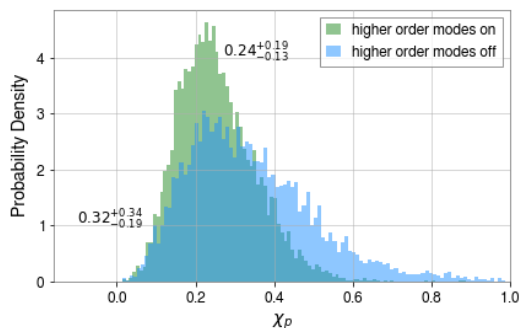

FIG. 21. Posterior probability density for χ_p using IM-RPhenomXPHM with and without higher-order multipoles. The values on the plot give the median and 90% confidence interval.

Due to the inclination of GW190412, the higher-order multipoles partially break the inclination and distance degeneracy which ultimately allows us to obtain tighter constraints on the inclination angle and distance. Fig. 22 shows the results obtained using IMRPhenomXPHM with higher-order multipoles while Fig. 23 is obtained excluding higher-order multipoles. Comparing the two, we see the degeneracy breaking as we include higher-order multipoles, despite the minor support for $\theta_{JN} > 1.7$.

C. Bayes Factor

To determine if the inclusion of higher-order multiples in the model fit the data more accurately than the dominant multipole model, we use Bayesian analysis. Specifically, we use the Bayes factor, $\log_{10} \mathcal{B}$, where $\mathcal{B}$ is the
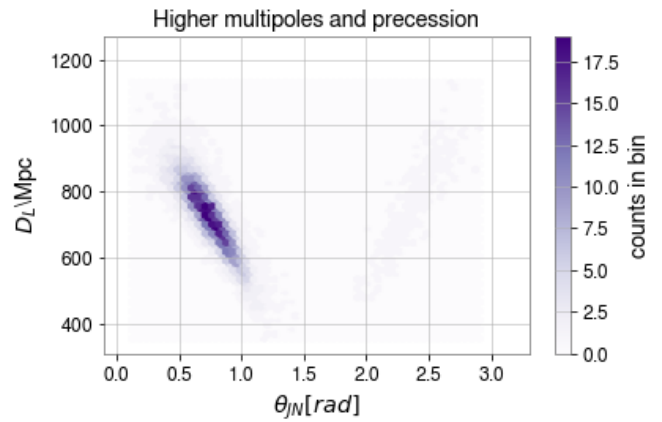

FIG. 22. The distance versus the inclination-angle inferred for GW190412 using IMRPhenomXPHM with higher-order multipoles and precession. As shown in this plot, the distance of GW190412 is inferred to be $\sim$700 Mpc or $\sim$ 2.3 billion light-years).
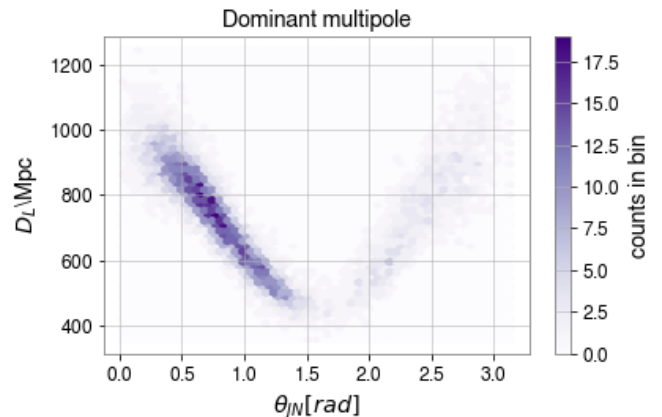

FIG. 23. The distance versus the inclination-angle inferred for GW190412 using IMRPhenomXPHM without higher-order multipoles. As shown in this plot, the distance of GW190412 is inferred to be $\sim$790 Mpc or $\sim$ 2.6 billion light-years).

ratio of signal and noise likelihoods, for different signal hypotheses [20]. We often use Bayes factors to provide quantitative support for one of the hypothesis over the other. For this study, I obtained $\log_{10} \mathcal{B}$=146.66 for the model including higher-order multipoles while $\log_{10} \mathcal{B}$=138.61 with the model excluding higher multipoles. This indicates evidence that GW190412 contained effects of higher-order multipoles.

VII. CONCLUSIONS

In this study, we investigated the properties of higher-order multipoles in gravitational waveforms emitted from binary black hole mergers. It is essential to have wave-

form models that include higher-order multipoles in order to accurately infer the astrophysical source properties of compact binary coalescences. Throughout this study, we noted that as the mode of the gravitational wave signal increases, the amplitude of the waveform decreases. In addition, the gravitational wave signal behaves accordingly to m which allows us to have a rough idea where the modes are located relative to one another in frequency.

Focusing on GW190412, detected in O3, we observed that due to the spin orbit precession, there is amplitude modulation in the waveform signal. GW190412 was an extremely important event that broke the near equal mass trend seen with events detected in previous LIGO / Virgo observing runs. As a result of the asymmetric component masses, the orientation of the binary can be determined more precisely as well as the measurements of the distance, mass ratio, and spin of the system. The results presented in Sec. VI show just how much of a greater impact higher-order multipoles have on constraining some of the source parameters. The high ratio of Bayes factors 10^8 for the study with higher multipoles provides evidence that signal includes quantitative imprints of higher multipoles.

Another task for this study is to use the waveform model, NRSur7dq4 to perform the same analysis. NR-Sur7dq4 is the newest surrogate model for binary black hole mergers and comparing those results with those from IMRPhenomXPHM would tell the degree to which our results depend on the waveform model (a crude estimate of the systematic error associated with the waveform model). As gravitational wave detectors become more sensitive, in the future we'll be able to observe events with high SNR which means that including higher-order multipoles in parameter estimation and tests of General Relativity will be essential.

VIII. ACKNOWLEDGMENTS

[1] B. P. Abbott *et al.* (LIGO Scientific Collaboration and Virgo Collaboration), Advanced LIGO, Classical and Quantum Gravity **32**, 074001 (2015), arXiv:1411.4547 [gr-qc].

[2] B. P. Abbott *et al.* (LIGO Scientific Collaboration and Virgo Collaboration), Advanced Virgo: A Second-Generation Interferometric Gravitational Wave Detector, Classical and Quantum Gravity **32**, 024001 (2014).

[3] B. P. Abbott *et al.* (LIGO Scientific Collaboration and Virgo Collaboration), GWTC-1: A Gravitational-Wave Transient Catalog of Compact Binary Mergers Observed by LIGO and Virgo during the First and Second Observing Runs, Phys. Rev. X **9**, 031040 (2019).

[4] B. P. Abbott *et al.* (LIGO Scientific Collaboration and Virgo Collaboration), Gravitational-Wave Candidate Event Database, https://gracedb.ligo.org/superevents/public/O3/.

[5] B. P. Abbott *et al.* (LIGO Scientific Collaboration and Virgo Collaboration), Prospects for Observing and Localizing Gravitational-Wave Transients with Advanced LIGO, Advanced Virgo and KAGRA (2020), arXiv:1304.0670 [gr-qc].

[6] B. P. Abbott *et al.* (LIGO Scientific Collaboration and Virgo Collaboration), GW190412: Observation of a Binary-Black-Hole Coalescence with Asymmetric Masses (2020), arXiv:2004.08342 [astro-ph.HE].

[7] B. Abbott, R. Abbott, T. Abbott, M. Abernathy, F. Acernese, K. Ackley, C. Adams, T. Adams, P. Addesso, R. Adhikari, and et al., Tests of general relativity with gw150914, Physical Review Letters **116**, 10.1103/physrevlett.116.221101 (2016).

[8] B. P. Abbott *et al.* (LIGO Scientific Collaboration and Virgo Collaboration), Binary black hole population properties inferred from the first and second observing runs of advanced ligo and advanced virgo, The Astrophysical Journal **882**, L24 (2019).

[9] B. P. Abbott *et al.* (LIGO Scientific Collaboration and Virgo Collaboration), A Gravitational-Wave Measurement of the Hubble Constant Following the Second Observing Run of Advanced LIGO and Virgo (2019), arXiv:1908.06060 [astro-ph.CO].

[10] B. S. Sathyaprakash and B. F. Schutz, Physics, Astrophysics and Cosmology with Gravitational Waves., Living Rev. Relativ. **12**, 10.12942 (2009).

[11] J. B. Hartle, *Gravity: An Introduction to Einstein's General Relativity*, illustrate ed. (Benjamin Cummings).

[12] L. London, S. Khan, E. Fauchon-Jones, C. García, M. Hannam, S. Husa, X. Jiménez-Forteza, C. Kalaghatgi, F. Ohme, and F. Pannarale, First Higher-Multipole Model of Gravitational Waves from Spinning and Coalescing Black-Hole Binaries, Physical Review Letters **120**, 10.1103/physrevlett.120.161102 (2018).

[13] S. Ossokine, A. Buonanno, S. Marsat, R. Cotesta, S. Babak, T. Dietrich, R. Haas, I. Hinder, H. P. Pfeiffer, M. Pürrer, C. J. Woodford, M. Boyle, L. E. Kidder, M. A. Scheel, and B. Szilágyi, Multipolar Effective-One-Body Waveforms for Precessing Binary Black Holes: Construction and Validation (2020), arXiv:2004.09442 [gr-qc].

[14] V. Varma, S. E. Field, M. A. Scheel, J. Blackman, D. Gerosa, L. C. Stein, L. E. Kidder, and H. P. Pfeiffer, Surrogate models for precessing binary black hole simulations with unequal masses, Physical Review Research **1**, 10.1103/physrevresearch.1.033015 (2019).

[15] Wikipedia, Gibbs phenomenon — Wikipedia, the free encyclopedia, `http://en.wikipedia.org/w/index.php?title=Gibbs%20phenomenon&oldid=959691031` (2020), [Online; accessed 07-July-2020].

[16] Sample release for gw190412, `https://dcc.ligo.org/LIGO-P190412/public/`.

[17] Antenna Patterns and Projecting a Signal into the Detector Frame, `https://pycbc.org/pycbc/latest/html/detector.html`.

[18] B. J. Owen, Search templates for gravitational waves from inspiraling binaries: Choice of template spacing, Physical Review D **53**, 6749–6761 (1996).

[19] B. Farr, D. E. Holz, and W. M. Farr, Using Spin to Understand the Formation of LIGO and Virgo's Black Holes, The Astrophysical Journal **854**, L9 (2018).

[20] Wikipedia, Bayes factor — Wikipedia, the free encyclopedia, `https://en.wikipedia.org/wiki/Bayes_factor` (2020), [Online; accessed 15-September-2020].

[21] B. P. Abbott *et al.* (LIGO Scientific Collaboration and Virgo Collaboration), GW190814: Gravitational Waves from the Coalescence of a 23 Solar Mass Black Hole with a 2.6 Solar Mass Compact Object, The Astrophysical Journal **896**, L44 (2020).

[22] G. Ashton, M. Hübner, P. D. Lasky, C. Talbot, K. Ackley, S. Biscoveanu, Q. Chu, A. Divakarla, P. J. Easter, B. Goncharov, and et al., Bilby: A User-friendly Bayesian Inference Library for Gravitational-wave Astronomy, The Astrophysical Journal Supplement Series **241**, 27 (2019).

[23] C. M. Biwer, C. D. Capano, S. De, M. Cabero, D. A. Brown, A. H. Nitz, and V. Raymond, PyCBC Inference: A Python-based Parameter Estimation Toolkit for Compact Binary Coalescence Signals, Publications of the Astronomical Society of the Pacific **131**, 024503 (2019).

[24] Gravitational-Wave Open Data Workshop #3, `https://www.gw-openscience.org/s/workshop3`.